J Solid State Electrochem (2012) 16:3621–3633
DOI 10.1007/s10008-012-1798-0

ORIGINAL PAPER

A facile and cost-effective synthesis of mesoporous $NiCo_2O_4$ nanoparticles and their capacitive behavior in electrochemical capacitors

Rui Ding · Li Qi · Hongyu Wang

Received: 15 May 2012 / Revised: 11 June 2012 / Accepted: 12 June 2012 / Published online: 26 June 2012

Abstract Mesoporous nickel cobaltite ($NiCo_2O_4$) nanoparticles were synthesized via a facile and cost-effective ball milling solid-state method and followed by a simple thermal treatment. The physical structures of the materials were characterized by X-ray diffraction, scanning electron microscopy, X-ray photoelectron spectrum, and Brunauer–Emmett–Teller methods. The electrochemical performances of the materials were investigated by cyclic voltammetry, chronopotentiomerty, electrochemical impedance spectra, and cycling life measurements. The physical characterizations show that the obtained materials consist of nanostructured $NiCo_2O_4$ spinels of hexagonal morphology and a spot of nanosized NiO spherical particles and display a layer-stacked mesoporous structure. Electrochemical measurements display that the $NiCo_2O_4$ electrode exhibits mainly a Faradaic pseudocapacitive behavior and possesses high performance even after 5,000 cycles with a specific capacitance value of 554 $F g^{-1}$ at 2 mV s^{-1} in 1 M KOH electrolytes, a power density and energy density respective value of 2,318 W kg^{-1} and 5.15 Wh kg^{-1} at a current density of 8 $A g^{-1}$ in 1 M KOH electrolytes, and an excellent cycling behavior with no capacitance decays and high coulombic efficiency close to 100 % during 5,000 cycles at a current density of 2 $A g^{-1}$ in 1 M KOH electrolytes, indicating a promising application for electrochemical capacitors.

R. Ding · L. Qi · H. Wang (✉)
State Key Laboratory of Electroanalytical Chemistry, Changchun Institute of Applied Chemistry, Chinese Academy of Sciences,
5625 Renmin Street,
Changchun 130022, China
e-mail: hongyuwang@ciac.jl.cn

R. Ding
Graduate School of Chinese Academy of Sciences,
Beijing 100039, China

Keywords Nickel cobaltite · Electrochemical capacitors · Pseudocapacitive · Mesoporous · Ball milling

Introduction

The depletion of traditional energy resources as well as the desire to reduce high CO_2 emissions associated with their use has led to significant interest in developing sustainable and clean energy products [1–4], such as electricity produced from wind- or solar-based technologies. As a result of the intermittent availability of these resources, the realization of their full potential will also require the development of new and advanced energy storage and delivery systems. Electrochemical capacitors (or supercapacitors), as a new class of energy storage devices, are now attracting intensive attention [2] because of their ability to store energy comparable to certain types of batteries, but with the advantage of delivering the stored energy much more rapidly than batteries [3]. This property makes electrochemical capacitors ideal to augment traditional batteries in many different applications. However, to become primary devices for power supply, electrochemical capacitors must be developed further to improve their abilities of energy density, power density, and long cycling life [5].

Regarding an electrochemical capacitor, the superiority of electrode materials is crucial for the clean, efficient, and versatile use of energy. Ruthenium oxide is a well-known electrode material with a high electrochemical reversibility and a high specific capacitance of over 700 $F g^{-1}$ [6, 7]. However, ruthenium oxide is very expensive and toxic. Thus far, various kinds of inexpensive transition metal oxides as electrode materials have been put forward for electrochemical capacitors, primarily including binary compounds of MnO_2 [8, 9], NiO [10, 11], Co_3O_4 [12, 13], etc.

It has been reported that nickel–cobalt binary metal oxides have greater electronic conductivity and

electrochemical activity than nickel and cobalt oxides [14]. Nickel cobaltite ($NiCo_2O_4$) is generally regarded as a mixed valence oxide that adopts a pure spinel structure in which nickel occupies the octahedral sites and cobalt is distributed over both octahedral and tetrahedral sites and is expected to offer richer redox chemistry than the two single component oxides due to the combined contributions from both nickel and cobalt ions, and it has been widely used in the fields of magnetic materials [15], electro-catalysts [16–19], optical limiters and switches [20], chemical sensors [21], and lithium ion batteries [22, 23]. Methods that have been also employed for the manufacture of nickel cobaltite nanoparticles, largely including hydroxide decomposition [24, 25], nanocasting [26], electrodeposition [27], combustion [28], coprecipitation [29], and the sol–gel synthesis [30, 31].

Very recently, Lu et al. [31] reported the novel epoxide-driven sol–gel process to prepare $NiCo_2O_4$ aero gels, exhibiting ultrahigh specific capacitances of 1,400 $F\,g^{-1}$. However, as much as we know, $NiCo_2O_4$ spinels have less drawn attention as electrode materials for electrochemical capacitors so far. A few current correlative papers can be indexed up to date [32–36]. Therefore, it is significant and challenging to exploit $NiCo_2O_4$ materials for electrochemical capacitors, and we have been attracted great research interests in these aspects.

In many applications, particle properties, such as size, surface area, and crystallinity, have a profound effect on the performance of the materials. Moreover, the synthetic method itself largely restricts the practical applications of obtained materials. Herein, we report a ball milling solid state and simple thermal treatment technique to synthesize mesoporous $NiCo_2O_4$ nanoparticles for electrochemical capacitors. In comparison with wet chemical processes, the ball milling technique is more cost-effective and easily scalable to mass production. To the best of our knowledge, there is no report on the synthesis of $NiCo_2O_4$ nanoparticles for electrochemical capacitors via this simple technique. The physical structures and electrochemical performances of as-synthesized materials were characterized and investigated, respectively. It is found that the obtained $NiCo_2O_4$ nanoparticles exhibit a high capacitance and excellent cycle behavior and thus a promising application in electrochemical capacitors.

Experimental

Synthesis of materials

All chemicals were of analytical grade and were used without further purification. The typical synthetic procedure is as follows: 8.4960 g $Co(NO_3)_6{\cdot}6H_2O$, 4.2480 g $Ni(NO_3)_6{\cdot}6H_2O$, and 5.2650 g NaOH (the molar ratio of total metal salts and alkali is 1:3, NaOH in excess) were milled in a planetary ball mill (QM-3SPO4, Nanjing) in a stainless steel vessel in air at the milling speed of 400 $r\,min^{-1}$. The ball-to-powder mass ratio was 5:1 and the duration of milling was 3 h. After milling, the samples were washed several times with distilled water and absolute alcohol, and subsequently dried in vacuum at 60 °C for 12 h. Through those procedures, the precursors were obtained. Finally, take some parts of the precursors which were calcined at 300 °C for 3 h in air atmosphere at a heating rate of 1 °C min^{-1} in a muffle stove to obtain the products.

Structural characterizations

Thermogravimetric analysis (TGA) and differential scanning calorimetry (DSC) were carried out with a STA 449 F3 Jupiter thermogravimetric analyzer (NETZSCH) in the temperature range from 40 to 810 °C in air at a heating rate of 10 °C min^{-1}. X-ray diffraction (XRD) patterns of the samples were recorded on a Rigaku-Dmax 2500 diffractometer equipped with graphite monochromatized Cu Kα radiation source (λ= 1.5418 Å) at a scanning speed of 4 °C min^{-1} in the range from 10° to 80°. Scanning electron microscopy (SEM) images were conducted using Philips XL 30 and a JEOL JSM-6700 F microscope. X-ray photoelectron spectrum (XPS) was measured by using an ESCALAB-MKII spectrometer (UK) with Al Kα radiation (1,486.6 eV) as the X-ray source for excitation, the raw spectra were curve-fitted by nonlinear least squares fittings with a Gauss–Lorentz ratio (60:40) using the XPS peak fit software, and the binding energies (BEs) were evaluated using C_{1s} spectrum (BE=284.6 eV) as reference with the accuracy of ±0.1 eV. Surface area and porosity were determined by nitrogen absorption at 77 K using a Micromeritics ASAP 2020 Analyzer; prior to analysis, all samples were degassed under vacuum at 120 °C for 4 h. The specific surface area was calculated using the Brunauer–Emmett–Teller (BET) method, while the pore size distribution, average pore diameter and pore volume were calculated from the desorption branches based on the Barrett–Joyner–Halenda equation using Quantachrome NOVA 4000e surface analyzer.

Fabrication of working electrode

The working electrodes were fabricated firstly by pressing the homogenized mixture of 66.7 % (in weight) active materials (as-synthesized $NiCo_2O_4$), 33.3 % (in weight) conductive agent and binder (teflonized acetylene black) on respective current collector (stainless steel mesh, 1 cm^2 area), and followed by drying in a vacuum oven at 80 °C for 12 h. The mass loading of active materials was usually controlled at 4 mg cm^{-2}.

Electrochemical performances tests and evaluation

The electrochemical performances of working electrode were examined using a cyclic voltammetry (CV) measurement by CHI700D electrochemical workstation, a galvanostatic charging–discharging or chronopotentiomerty (CP) test via LandCell^{TM} tester and an electrochemical impedance spectra (EIS) experiment through Par Sta. 2273 electrochemical complex instrument.

Tests for working electrode were carried out in a conventional three-electrode electrochemical setup which comprises a $NiCo_2O_4$ working electrode, a platinum plate (2×2 cm) counter electrode, and a Hg/HgO (1 M KOH, aqueous) reference electrode. CV tests were usually cycled between the voltage of 0 and 0.6 V with scan rates ranged from 2 to 100 mV s^{-1}, CP measurements were generally cycled between the voltage of 0 and 0.6 V with charging–discharging rates or current densities varied from 0.5 to 8 A g^{-1}, EIS experiments were taken under a constant direct current bias potential of open-circuit voltage with a alternating current (AC) amplitude of 5 mV over the sinusoidal alternating voltage frequency range from 10^{-2} to 10^5 Hz. Cycle life test was conducted via a CP measurement between 0 and 0.6 V at a current density of 2 A g^{-1} for 5,000 cycles. During all tests, 1 M KOH aqueous solution was chosen as electrolyte. All tests were carried out at room temperature.

The gravimetric specific capacitance (C_m, F g^{-1}) values determined from the CV curves were calculated according to Eq. (1):

$$C_m = \frac{1}{\mathrm{vm}(\Delta V)} \int_{V_a}^{V_b} I \mathrm{d}V \tag{1}$$

Where v (millivolts per second) is scan rate, ΔV (volt) is the applied potential window (V_a to V_b) and m (gram) is the mass of the active materials in working electrode.

The gravimetric specific capacitance (C_m, Femtogram per gram), energy density (E_m, Watt hour per kilogram), power density (P_m, Watt per kilogram), and coulombic efficiency (η, percent) all values measured from the CP curves were calculated according to Eqs. (2)–(5):

$$C_m = \frac{I\Delta t_d}{m(\Delta V)} = \frac{i\Delta t_d}{\Delta V} \tag{2}$$

$$E_m = \int \mathrm{V}\mathrm{d}q_m = \frac{1}{2} C_m (\Delta V)^2 \tag{3}$$

$$P_m = \frac{E_m}{\Delta t_d} = \frac{I\Delta V}{2m} \tag{4}$$

$$\eta = \frac{\Delta t_\mathrm{d}}{\Delta t_\mathrm{c}} \times 100 \tag{5}$$

Where I (A) and i (A per gram) are respective charging–discharging current and current density, ΔV (volts) is the applied potential range, Δt_d and Δt_c are the time of discharging and charging respectively, and m (gram) is the mass of the active materials in working electrode.

Results and discussion

Structural characteristics of $NiCo_2O_4$ materials

TGA–DSC are effective techniques to measure both weight changes (TGA) and heat flow (DSC) as a function of temperature or time in a controlled atmosphere. Herein, TGA–DSC measurements were carried out to investigate the thermal behavior of the Ni-Co hydroxides precursor in air. As illustrated in Fig. 1, there are four distinct weight loss steps in thermogravimetric (TG) plots. The first step (3.8 % weight loss) occurs in the temperature range between 40 and 141.5 °C with an endothermic peak in the DSC curves, corresponding to the evaporation of physical adsorbed water. The second step (15.3 % weight loss) occurs in the temperature range between 141.5 and 398.7 °C with two continuous but difform exothermic peaks marked as peak 1 (188.9 °C) and peak 2 (302.2 °C), respectively, in the DSC curves, which is probably caused by the difference of reaction rate during conversion process of precursor. The two exothermic peaks associate with thermal decomposition of the Ni-Co hydroxides precursor powders to formation of $NiCo_2O_4$ spinels, and a very minor amount of NiO as a result

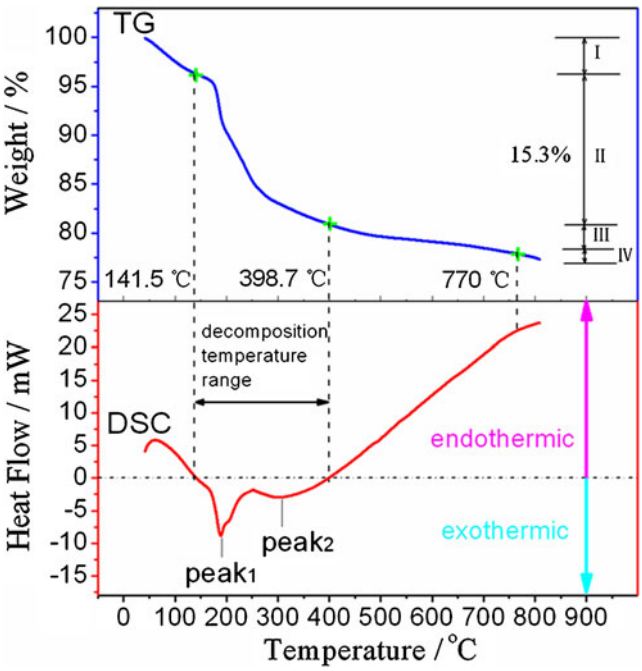

Fig. 1 TG and DSC curves of precursor

of incomplete homogenousity in precursor which caused the slight excess of Ni hydroxides (the existence of NiO can be validated by SEM and XRD discussed later). The low-grade impurity of $NiCo_2O_4$ materials here is not surprising, similar phenomenon can be found in the reported paper by Lu et al. [31], where nickel cobaltite aerogel crystalline phase was accompanied by a very minor amount of $Ni(OH)_2$ crystalline phase. The overall conversion reactions are expressed as Eqs. (6) [37] and (7):

$$Ni(OH)_2 + 2Co(OH)_2 + \frac{1}{2}O_2 \rightarrow NiCo_2O_4 + 3H_2O \quad (6)$$

$$Ni(OH)_2 \rightarrow NiO + H_2O \quad (7)$$

Note that the overall weight loss (15.3 %) of the second step is slightly larger than the theoretical conversion value (13.6 %) of $NiCo_2O_4$, which can also be accounted for by the conversion of NiO (20 % weight loss in theoretical). The third step (3.1 % weight loss) occurs in the temperature range varying from 398.7 to 770 °C with a broad endothermic peak in the DSC curves, owing to decomposition of the $NiCo_2O_4$ spinels [38]. The fourth step (0.47 % weight loss) begins with 770 °C with an endothermic peak in the DSC curves, owing to decomposition of the Co_3O_4 [39]. On the basis of the TGA–DSC results, the temperature for calcinations was set at 300 °C for 3 h to ensure complete decomposition of the precursor.

XRD technique is a very useful tool to determine the phase, crystallinity, and purity of materials. Figure 2 shows the typical XRD patterns of $NiCo_2O_4$ materials. The resultant diffraction peaks basically corroborate with the standard patterns for cubic $NiCo_2O_4$ (JCPDS no. 73–1702) with spinel structure, but two unnoticeable weak shoulder peaks of cubic NiO (JCPDS no. 73–1579) are also detectable, indicating that the $NiCo_2O_4$ materials coexist with a spot of cubic NiO as impurity phase comes into being, which are consistent with the result of TGA and observation of SEM. The largely sharp and defined diffraction lines illustrate good crystallinity of the materials, which agrees well with the SEM result. The lattice parameter a_0 of the materials determined from the observed d-spacing for crystal plane (311) at 2θ value of 36.95° by using Eqs. (8) and (9) for a cubic lattice is 0.8067 nm, which is less than the standard value of 0.8110 nm for $NiCo_2O_4$ (JCPDS 20–0781). Beyond some errors in the determination of Bragg angles associated with the broad diffraction lines of the patterns, it may be explained by the existence of NiO, which is the same as the deviation phenomenon reported in the literature [37].

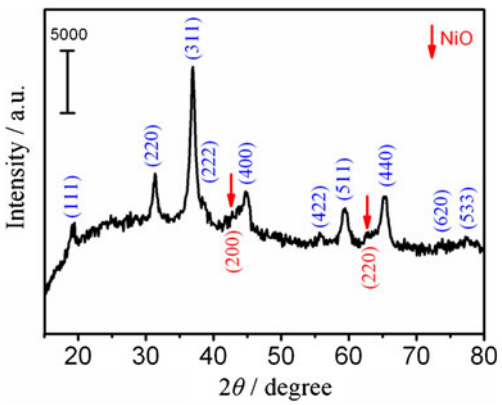

Fig. 2 XRD patterns of $NiCo_2O_4$ materials

$$a_0 = d\left(h^2 + k^2 + l^2\right)^{\frac{1}{2}} \quad (8)$$

$$2d \sin\theta = \lambda \quad (9)$$

Where λ is the wavelength of X-ray radiation (1.5418 Å); θ is the Bragg angle of diffraction; d is observed space for crystal plane; h, k, and l are the Miller indices.

The SEM images of $NiCo_2O_4$ materials are shown in Fig. 3a, b. The observed $NiCo_2O_4$ particles have a layer-stacked structure and a hexagonal shape with an average diameter of about 220 nm. Note that a few spherical particles identified as cubic NiO (JCPDS no. 73–1579) with a diameter range of about 80–150 nm can be found in the figure, indicating the $NiCo_2O_4$ materials mix a spot of cubic NiO as impurity, which corresponds well with XRD analysis

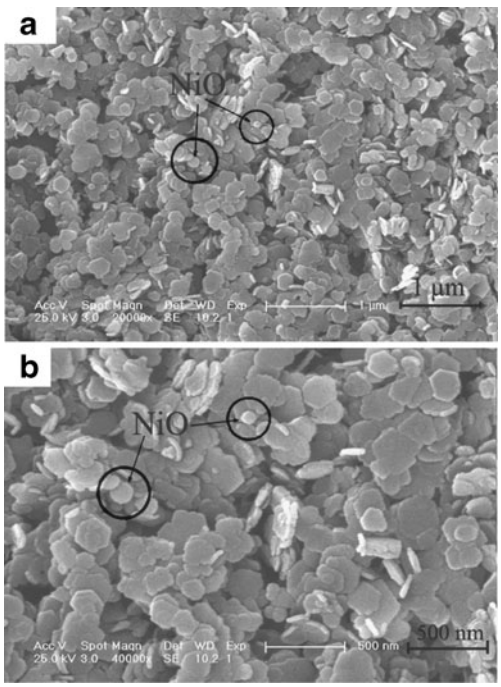

Fig. 3 SEM images of $NiCo_2O_4$ materials at different magnifications: 1 μm (**a**) and 500 nm (**b**)

and TGA result. In addition, the material consists of layered-stacked porous structure of the particles and this can provide easy access for ions to access the electrode/electrolyte interface, which is a very important factor for the Faradaic surface reactions in electrochemical capacitors.

The chemical bonding states of each element on the surface of $NiCo_2O_4$ materials were evaluated by XPS. Figure 4a displays the full-scan spectra of the materials, which mainly contains C_{1s} (as reference), O_{1s}, Co_{2p}, and Ni_{2p} four core levels peaks. Of which, O_{1s} spectra exhibit three main peaks at 532.9, 531.2, and 529.4 eV shown in Fig. 4b, associating with hydroxyl species of surface-adsorbed water molecule [40], oxygen ions in low coordination at the surface, and the typical of metal–oxygen bonds [41], respectively. The Co_{2p} spectra shown in Fig. 4c consist of two spin-orbit doublets characteristic of Co^{2+} and Co^{3+}, and two shakeup satellites (identified as "Sat."). Similarly, the Ni_{2p} spectra given in Fig. 4d are composed of two spin-orbit doublets characteristic of Ni^{2+} and Ni^{3+} and two shakeup satellites. These results show that the surface of the as-synthesized $NiCo_2O_4$ materials has a composition containing Co^{2+}, Co^{3+}, Ni^{2+}, Ni^{3+}, and O^{2-}, which is in good agreement with the results in the literature for $NiCo_2O_4$ spinels [40–42].

BET measurements are carried out to study the specific surface areas and the pore structure of $NiCo_2O_4$ materials. Typical nitrogen adsorption/desorption isotherms, corresponding pore size distribution and pore volume plots of the materials are shown in Fig. 5a–c. As shown in Fig. 5a, the nitrogen sorption isotherms of the materials can be classified as type IV with H3 type hysteresis loop behavior according to the International Union of Pure and Applied Chemistry classification, typical mesoporous materials. Meanwhile, the hysteresis loop is associated with the secondary process of capillary condensation, which starts at about P/P_0=0.5 and expends almost to P/P_0=1, suggesting complete filling of the mesopores and a high fraction of textual porosity of the materials, which is in well agreement with SEM observations. The specific surface area, cumulative pore volume, and average pore diameter of the materials is 125.7 $m^2\ g^{-1}$, 0.6762 $cm^3\ g^{-1}$, and 21.5 nm, respectively. Moreover, pore size exhibits a trimodal size distribution at 2.7, 5.6, and 31 nm due to expansion of pores and with the majority of the pores basically falling in the optimal sizes of 2–5 nm for electrochemical capacitors applications [43–45].

Note that both highly porous structure and large surface area of electrode material are beneficial to performance of electrochemical capacitors. The porosity determines ion transfer rate in electrode and the extent of electrode/electrolyte interfacial area. Surface area is contributed to electric double layer capacitance (C_{EDL}). The C_{EDL} of the materials provided by surface area can be estimated by Eq. (10), the

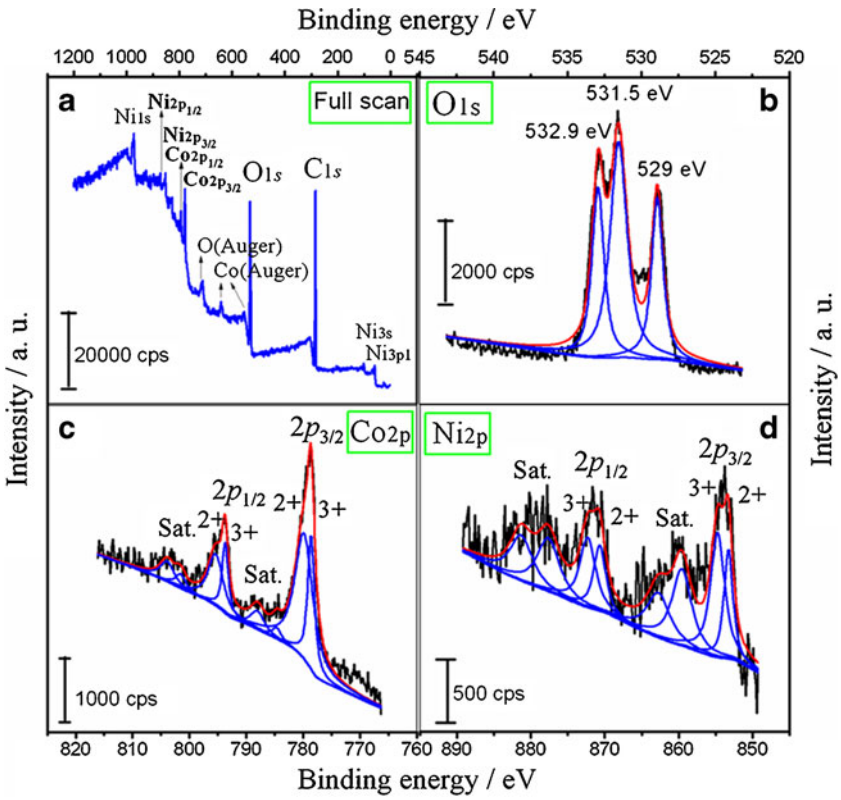

Fig. 4 XPS spectra of $NiCo_2O_4$ materials: full-scan (**a**), O_{1s} core levels (**b**), Co_{2p} core levels (**c**), and Ni_{2p} core levels (**d**)

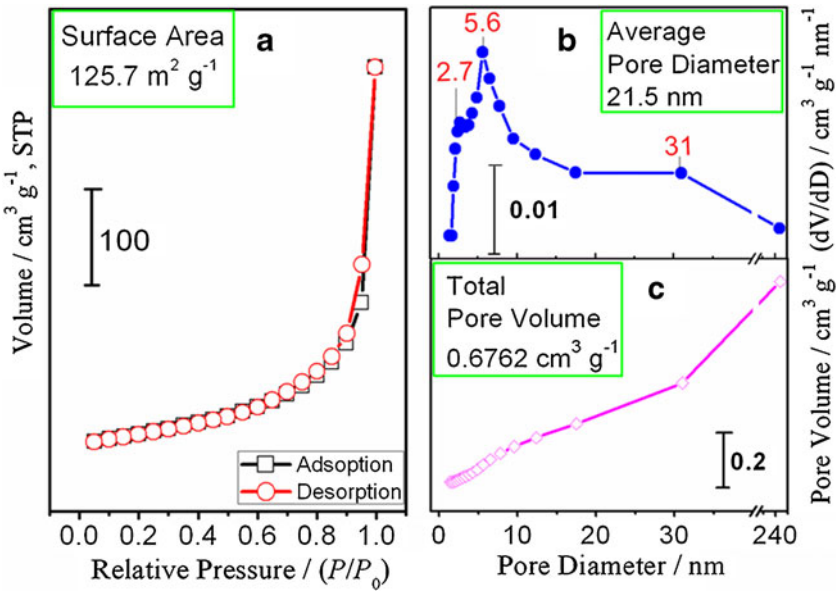

Fig. 5 BET plots of $NiCo_2O_4$ materials: nitrogen adsorption/desorption isotherms (**a**), pore size distribution (**b**), and pore volume distribution (**c**)

value is just 25.14 Fg^{-1}, implying main pseudocapacitive behavior of $NiCo_2O_4$ spinels.

$$C_{EDL} = C_{STD} \times S_{BET} \quad (10)$$

Where C_{STD} represents capacitance per unit real surface area and its value equals to 20 μF cm^{-2}, S_{BET} is the surface area measured by BET method.

Electrochemical performances of $NiCo_2O_4$ electrode

CV is a very useful tool to determine various electrode processes, electrode reaction mechanisms, reversibility, dynamic parameters, etc. Figure 6 shows CV performances of $NiCo_2O_4$ electrode. As shown in Fig. 6a, there are three distinct areas in the whole CV plots, an electric double layer (EDL) area (0–0.12 V), a redox reaction area (0.12–0.58 V), and an irreversible oxygen evolution reaction (OER) area (~0.6 V). In EDL area, a small and approximately constant response of current density appears with the change of scanning potential, indicating no redox reactions occur in this area, which reflects the charge storing/releasing conduct of various charged particles at the electrode/electrolyte interface, mainly the conduct of charged particles of ionic EDL. In redox reaction area, one pair of broad peak marked as (A_1, C_1) can be observed, which can be identified as redox couple Co^{3+}/Co^{2+} [31, 33, 37], whereas no obvious signal of redox couple Ni^{3+}/Ni^{2+} appears, the reason maybe that the content of NiO is relatively low in the materials, and meanwhile its peak position just places on the shoulder of Co^{3+}/Co^{2+}, as a result, it is covered by the peak Co^{3+}/Co^{2+}. In OER area, there appears one cone-shaped peak, corresponding to OER reaction (4 $OH^- \rightarrow 2\ H_2O + O_2$), indicating high OER electrocatalytic property of the $NiCo_2O_4$

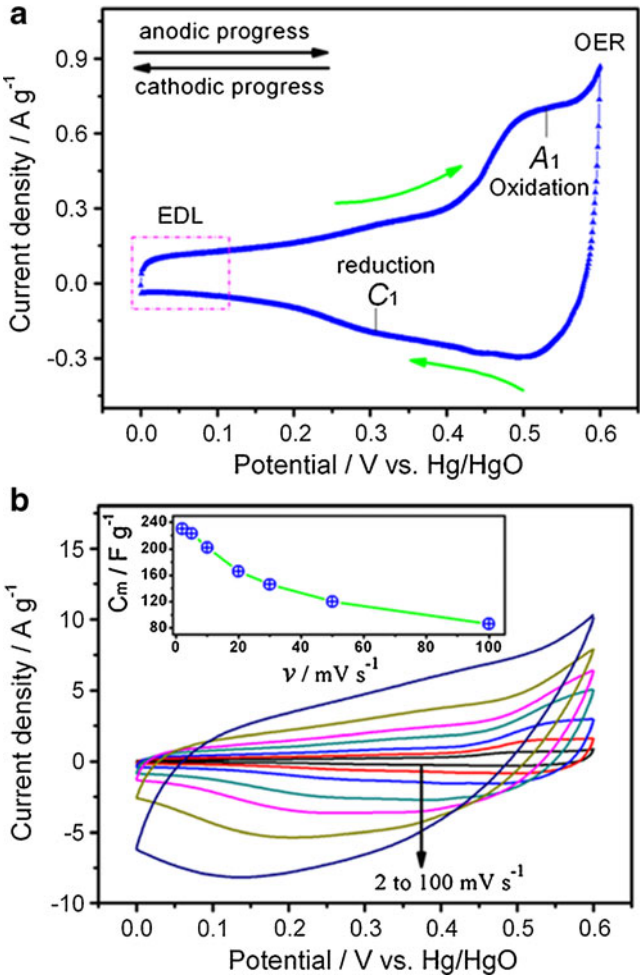

Fig. 6 CV performances of $NiCo_2O_4$ electrode: CV plots at a scan rate of 2 mV s^{-1} (**a**) and CV plots at different scan rates (**b**; *inset* shows the variations of C_m with v)

materials and the potential window of $NiCo_2O_4$ electrode can be no more than 0.6 V under the testing conditions.

The capacitive property of electrode materials can be also judged from CV plots. According to the plots, the capacitance of $NiCo_2O_4$ electrode include EDL capacitance (C_{EDL}) and Faradaic pseudocapacitance (C_F), which produce the respective CV curves close to an ideal rectangular shape and redox peaks respectively. Evidently, the $NiCo_2O_4$ electrode mainly shows pseudocapacitive performance, because the integral area of redox peaks is far more than that of rectangle. Based on above analysis, the overall electrochemical reactions of $NiCo_2O_4$ electrode could be expressed as Eqs. (11) [46], (12) [47].

$$NiCo_2O_4 + OH^- \rightleftarrows NiCo_2O_4\|OH^- + NiCo_2O_4 - OH \quad (11)$$

$$NiO + xOH^- \rightleftarrows xNiOOH + (1-x)NiO + xe^- \quad (12)$$

Where $NiCo_2O_4\|OH^-$ represents the EDL formed by the hydroxyl ion, and $NiCo_2O_4$-OH represents the product formed by oxidation reaction involving the hydroxyl ion.

Figure 6b shows CV plots at different scan rates and corresponding C_m values calculated according to Eq. (1), which exhibits a value range from 230 to 86 $F\,g^{-1}$ at the scan rate range from 2 to 100 mV s^{-1}. The decrease of the capacitance with the increase the scan rate is caused mainly by the existent of electrochemical reaction resistance (R_e) of the electrode that resulted serious electrochemical polarization and produced relatively insufficient Faradaic redox reactions of the active materials under high scan rates. Usually, the specific capacitance obtained at the slowest scan rate is more close to that of full utilization of the active materials of the electrode.

The electrochemical behavior of $NiCo_2O_4$ electrode was also examined by CP test. Figure 7a, b shows CP plots of the first three cycles and the first cycle of $NiCo_2O_4$ electrode at the current density of 0.5 $A\,g^{-1}$, respectively. Consistent with the CV plots of Fig. 6a essentially, the whole CP plots can be also divided in to three clear areas, i.e. an EDL linear area (0–0.25 V), a redox reaction plateau area (0.25–0.55 V) marked as (I and II) and a OER cone-shaped peak area (~0.6 V), which associate with the charge storing/releasing conduct mainly originated from ionic EDL, the mutual conversions between redox couple Co^{3+}/Co^{2+}, and irreversible OER reaction at the electrode/electrolyte interface respectively. And also no obvious signal of redox couple Ni^{3+}/Ni^{2+} appears as a result of the coverage by Co^{3+}/Co^{2+}.

Like the CV method, CP measurement can be also used to determine the capacitive property of electrode materials. The CP plots in Fig. 7a, b show that the capacitance of $NiCo_2O_4$ electrode include C_{EDL} and C_F, which produces the respective CP curves with a linear and with a plateau relationship between potential and time, originating from EDL charging/discharging processes and interface redox reactions, respectively. Undoubtedly, the $NiCo_2O_4$ electrode displays mainly pseudocapacitive performance, because the charging/discharging time of plateau is far more than that of straight line.

Figure 7c shows the discharging branches of CP plots at different scan rates and corresponding C_m values calculated according to Eq. (2), which exhibits a value range varying from 126 to 193 $F\,g^{-1}$ when the current density changes from 0.5 to 8 $A\,g^{-1}$. Interestingly, the specific capacitance of

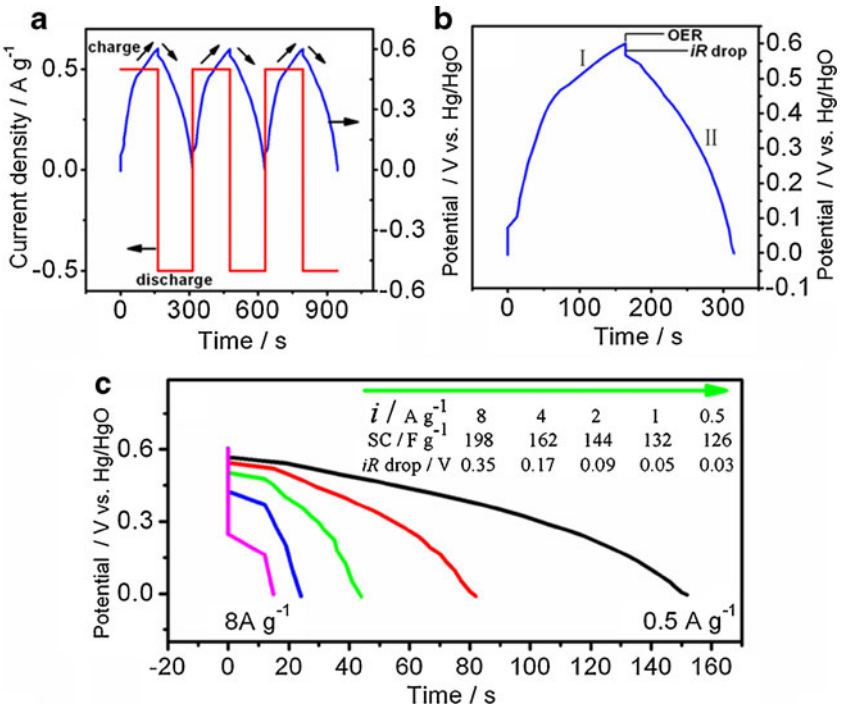

Fig. 7 CP performances of $NiCo_2O_4$ electrode: CP plots of the first three cycles at the current density of 0.5 $A\,g^{-1}$ (**a**), CP plots of the first cycle at the current density of 0.5 $A\,g^{-1}$ (**b**) and discharging branches of CP plots at different current densities (**c**; *inset* shows the variations of C_m as a function of i, note: all C_m values were calculated by applying a full potential window of 0.6 V, without deducting iR drop)

the $NiCo_2O_4$ electrode shows an ascending trend with the increase of current density, the reason is that the $NiCo_2O_4$ spinels are typical lattice-embedded materials and have large parts of reactive sites that cannot be used in fresh state. It needed to be activated before achieving more utilization of its capacitance and reaching a more stable state, the phenomenon is also demonstrated by other literature [31, 48, 49].

Here, the accessible reactive sites values (Z) of the $NiCo_2O_4$ electrode determined from CP plots can be estimated using the Eq. (13) [50]. The Z value changes from 0.188 to 0.288 when current density ranges from 0.5 to 8 A g^{-1}, indicating far nonfull-reactive sites generated in fresh state and the capacitance relaxation property of the $NiCo_2O_4$ electrode.

$$Z = \frac{C_m M \Delta V}{F} \tag{13}$$

Where C_m, ΔV, M, and F correspond to specific capacitance determined from CP plots, potential window (volt), molecular weight of $NiCo_2O_4$ (240.55 g mol^{-1}), and Faradic constant (96,487 C mol^{-1}).

Long cycling life is a very important factor for the electrode materials used in electrochemical capacitors. Figure 8 shows the cycling behavior of the $NiCo_2O_4$ electrode at a current density of 2 A g^{-1}. As demonstrated in the figure, the capacitance exhibits an ascending trend during all cycling numbers, the C_m value increased from 138 F g^{-1} of the first cycle to 207 F g^{-1} of the 500th cycle, then to 255 F g^{-1} of the 2,500th cycle, and last to 276 F g^{-1} of the 5,000th cycle, a 100 % increasing magnitude in total happened from the first cycle to the end of cycle, indicating the capacitance relaxation of the $NiCo_2O_4$ electrode which needs activation for at least 500 cycles under examined conditions before reaching a more stable state and more effective utilization of its capacitance. On the other hand, the coulombic efficiency of the electrode during all cycling periods maintained nearly at 100 %, showing an excellent reversibility of the $NiCo_2O_4$ electrode, implying a practical application for the electrochemical capacitors.

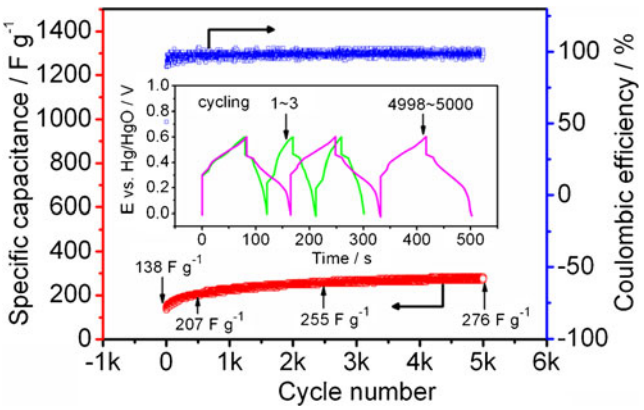

Fig. 8 Cycle life of $NiCo_2O_4$ electrode at a current density of 2 A g^{-1} (*inset* shows CP curves for cycles from first to third and 4,998–5,000th)

EIS is a very important tool to understand electrochemical behavior of electrode materials. Figure 9 shows EIS plots of the $NiCo_2O_4$ electrode in fresh and after 5,000 CP cycles. As shown in Fig. 9a, the Nyquist plots consist of a semicircle in the high frequency range and a declined line deviating 90° in the low-frequency area, corresponding to R_e and the deviation to pure capacitor of the electrode respectively. However, the Nyquist plots after 5,000 cycles exhibits a larger semicircle and a more deviated angle,

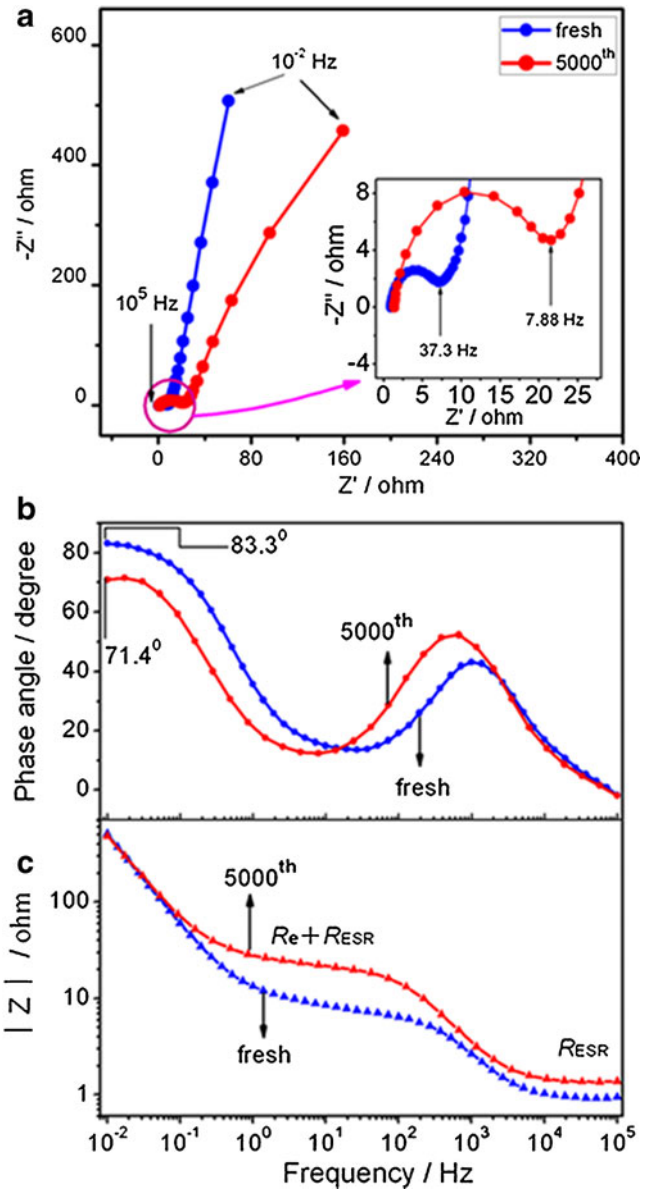

Fig. 9 EIS performances of $NiCo_2O_4$ electrode in fresh and after 5,000 CP cycles: Nyquist plots or complex plane impedance plots (**a**; *inset* shows the enlarged Nyquist plots at the high frequency region), Bode plots of phase angle vs. frequency (in logarithmic scale; **b**), and Bode plots of impedance (in logarithmic scale) vs. the frequency (in logarithmic scale; **c**)

associating with larger electrochemical polarization and more close to battery behavior of the electrode. The inset in Fig. 9a shows the charge saturation point of the electrode, a frequency response property and a measure of the power capability of an electrochemical capacitor. The frequency value after 5,000 cycles is 7.88 Hz, which is smaller than the value (37.3 Hz) of the fresh electrode, indicating more capacitance relaxation and worse power of the electrode materials after long cycles. The much loss of line with slope of 45° in the medium frequency region in both states suggests that Warburg resistance is not the determined factor in the electrode process and electrolyte ions can diffuse fast into the electrode, indicating high porous structure of the electrode materials. The approximate equal intercept of real axis of impedance in the super-high frequency (10^5 Hz) in both states reveals that the R_{ESR} of the electrode is not nearly influenced by long cycles. All discussed above can be further validated by the Bode plots of phase angle and impedance with frequency shown in Fig. 9b, c.

It has been studied for various cell assemblies based on the analysis of complex capacitance and complex power using impedance data by other workers [51–53]. Figure 10a, b show the complex capacitance [$C(\omega)$] and the complex power [$S(\omega)$] plots of the $NiCo_2O_4$ electrode with frequency, respectively. At low frequency, $C'(\omega)$ corresponds to the capacitance of the electrode materials and $C''(\omega)$ corresponds to the energy dissipation by an irreversible process that leads to a hysteresis [52]. As shown in Fig. 10a, the $C'(\omega)$ decreases as the frequency increases, and the capacitance value is nearly to zero at high frequency, which is characteristic of the electrode structure and electrode/electrolyte interface. The $C''(\omega)$ plots show a peak formation at low frequency, indicating a characteristic hysteresis for the electrode studied. The electrode shows a specific capacitance value of 32 $F g^{-1}$ (in fresh) and 36 $F g^{-1}$ (after 5,000 cycles) based on the respective $C'(\omega)$ plots, which is much smaller than the values obtained using CV and CP methods. However, this discrepancy should perhaps not be surprising as other workers have observed similar behavior for metal (Fe, Co, and Ni) oxides [54], and for lots of conducting polymers [55–58]. These workers have attributed the discrepancy to several factors such as slow conformational changes occurring in the polymer network [55, 56], the involvement of some physical and chemical heterogeneities [57], deeply trapped counter ions which remain immobile during impedance experiment [58], etc.

The frequency corresponding to the half of maximum value of $C'(\omega)$ and the maximum of $C''(\omega)$, known as the resonance frequency f_0, from which the relaxation time constant, $\tau_0(=1/2\pi f_0)$, can be estimated. In addition, from the crossing of normalized active power ($|P|/|S|$) and reactive power ($|Q|/|S|$) plots shown in Fig. 10b, f_0 and τ_0 can be also determined explicitly. The relaxation time constant is known as the dielectric relaxation time of the electrochemical capacitor [59], and is a figure of merit of an electrochemical capacitor. This parameter represents the transition of the electrochemical capacitor from purely resistive to purely capacitive behavior. For a frequency, $f>1/\tau_0$, it acts as a pure resistor and for $f<1/\tau_0$, it behaves as a pure capacitor. Based on the respective value of f_0 (0.64 and 0.21 Hz) for the two states, the value of τ_0 has been calculated to be 250 ms for the fresh electrode, and 770 ms for the electrode after 5,000 cycles. These values are not so short, indicating some extent relaxation of the electrode to delivery of stored energy at a high power, and the performances of the electrode are more close to that of batteries based on redox reactions. However, considering that even the most commercially available electrochemical capacitors, including those specifically designed for higher power applications, operate at frequencies less than 1 Hz (corresponding response time is 1,000 ms), the response time of this electrode is also considerable.

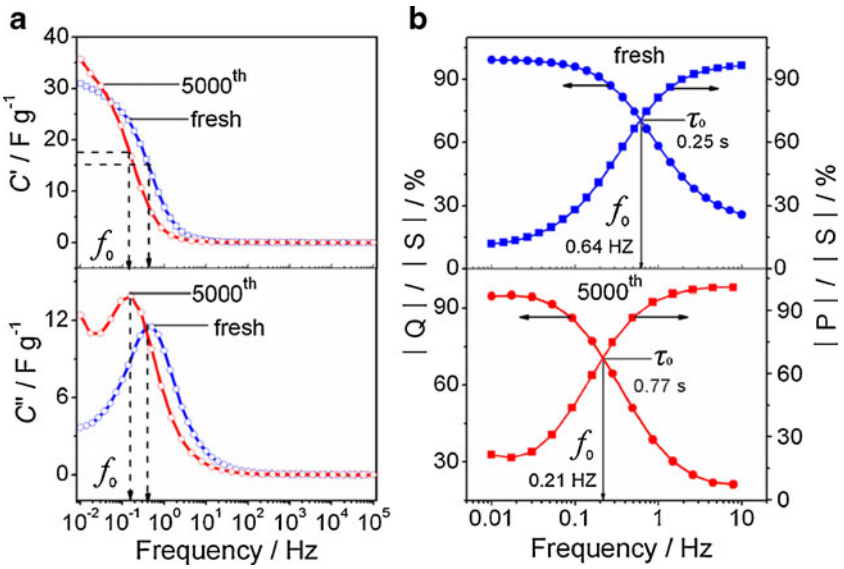

Fig. 10 Complex capacitance [$C(\omega)$] and complex power [$S(\omega)$] analysis of $NiCo_2O_4$ electrode in fresh and after 5,000 CP cycles: plots of complex capacitance of real part [$C'(\omega)$] and imaginary part [$C''(\omega)$] with the frequency (in logarithmic scale; **a**) and plots of normalized active power ($|P|/|S|$) and reactive power ($|Q|/|S|$) vs. frequency (in logarithmic scale; **b**)

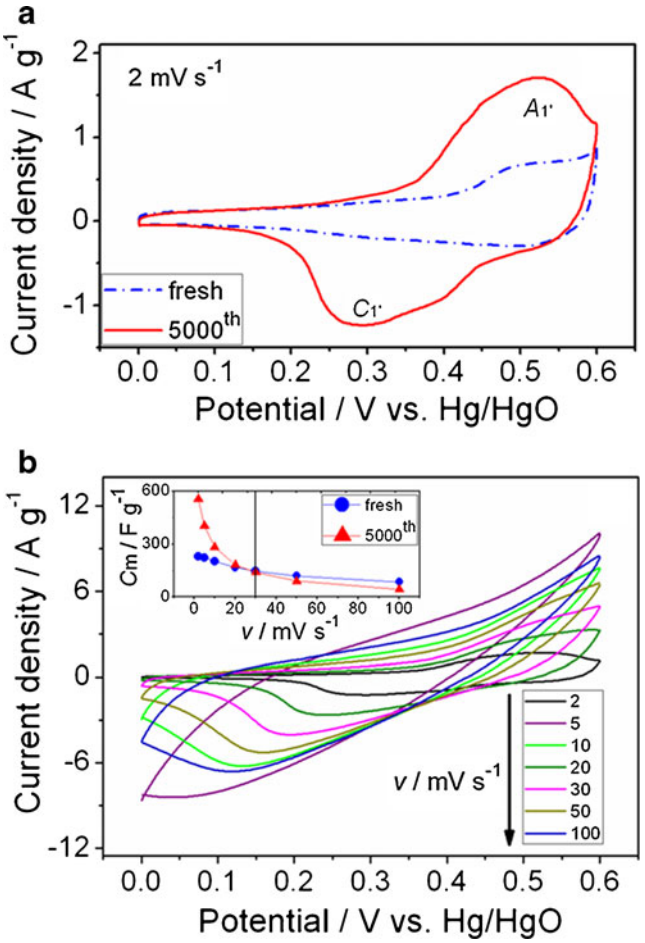

Fig. 11 CV performances of $NiCo_2O_4$ electrode after 5,000 cycles: CV plots at scan rates of 2 mV s^{-1} (**a**), and CP plots at different scan rates (**b**; *inset* shows C_m values as a function of different v conditions)

The calculations of complex capacitance and complex power conducted based on Eqs. (14)–(20):

$$Z(\omega) = Z'(\omega) + jZ''(\omega) \tag{14}$$

$$C(\omega) = C'(\omega) + jC''(\omega) \tag{15}$$

$$C'(\omega) = -Z''(\omega)/\omega|Z(\omega)|^2 \tag{16}$$

$$C''(\omega) = Z'(\omega)/\omega|Z(\omega)|^2 \tag{17}$$

$$S(\omega) = P(\omega) + jQ(\omega) \tag{18}$$

$$P(\omega) = \omega C''(\omega)|\Delta V_{\mathrm{rms}}|^2 \tag{19}$$

$$Q(\omega) = \omega C'(\omega)|\Delta V_{\mathrm{rms}}|^2 \tag{20}$$

Where $P(\omega)$, the active power, is the real part of the complex power, $Q(\omega)$, the reactive power, represents the imaginary part of the complex power, $|\Delta V_{\mathrm{rms}}|^2 = \Delta V_{\max}/\sqrt{2}$, $\Delta V_{\max}$ is the maximal amplitude of the AC signal, $C'(\omega)$ is the real part of the complex capacitance and $C''(\omega)$ is the imaginary part of the complex capacitance, $Z'(\omega)$ and $Z''(\omega)$ are the respective real and imaginary parts of the complex impedance $Z(\omega)$, ω is the angular frequency and it is given by $\omega = 2\pi f$.

CV performances of $NiCo_2O_4$ electrode after 5,000 CP cycles were investigated. As shown in Fig. 11a, after 5,000 CP cycles, the CV plots exhibit a pair of more strong redox peaks marked as (A'_1, C'_1) than the fresh electrode, associating with long cycling activation which generated far more available reactive sites (Z=0.829) than that (Z=0.344) of fresh electrode. Figure 11b shows that the CV plots display nearly a center-symmetric images between anodic and cathodic processes and a fast current–potential (i–V) response at a moderate scan rate (less than 30 mV s^{-1}), however, the CV performances become worse with further increase of scan rates, embodying that anodic peaks overlapped and even

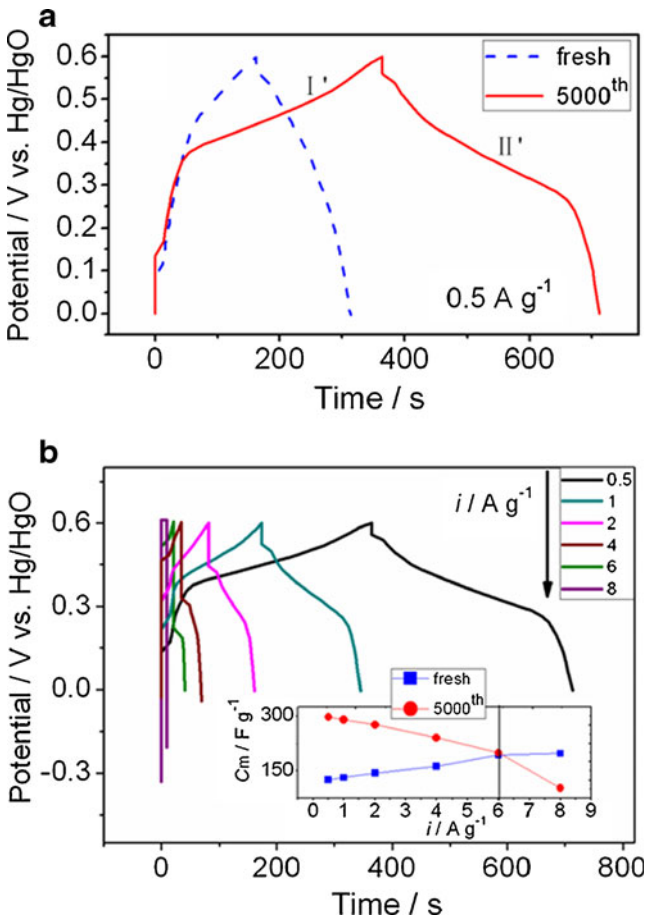

Fig. 12 CP performances of $NiCo_2O_4$ electrode after 5,000 cycles: CP plots at current density of 0.5 A g^{-1} (**a**) and CP plots at different current densities (**b**; *inset* shows C_m values as a function of different i conditions)

disappeared and cathodic peaks shifted toward negative potential gradually, and *i–V* response happened more and more slowly, mainly because the R_e and resultant electrochemical polarization of the electrode increased a lot after 5,000 CP cycles.

The inset of Fig. 11b shows a C_m value range from 554 to 44 $F g^{-1}$ at the scan rate range varying from 2 to 100 mV s^{-1}. Moreover, the C_m values shows a boundary at a scan rate of 30 mV s^{-1} in comparison with the C_m values of fresh electrode, when the scan rate is less than 30 mV s^{-1}, the C_m values are larger than that of fresh electrode, and the situation are contrary when the scan rate is more than 30 mV s^{-1}, corresponding well with the changes of the CV plots discussed above.

CP performances of $NiCo_2O_4$ electrode after 5,000 CP cycles were also investigated. As shown in Fig. 12a, the CP plots after 5,000 CP cycles display a pair of more distinct and longer redox reaction charging/discharging plateau marked as (I′, II′) than the fresh electrode, resulting from the obtained more reactive sites after long cycling activation, the *Z* value increased from 0.188 (fresh) to 0.444 (5,000th) at the current density of 0.5 $A g^{-1}$. As shown in Fig. 12b, it largely displays a center-symmetric property between charging and discharging branches and a low *iR* drop at a current density of no more than 6 $A g^{-1}$, whereas with further increase of current density, the two branches become asymmetry and even distorted (for example, the CP plots become a pulse form at 8 $A g^{-1}$), and meanwhile the influence of *iR* drop becomes evident, indicating large R_e and unignored R_{ESR} of the $NiCo_2O_4$ electrode under high charging/discharging rates, which corresponds with CV performances of the electrode.

The C_m values given in inset of Fig. 12b show a range from 297 to 103 $F g^{-1}$ when the current density ranges from 0.5 to 8 $A g^{-1}$. In addition, the C_m values exhibit a boundary at a current density of 6 $A g^{-1}$ comparing with fresh electrode, when the current density is less than the boundary, the C_m values are larger than that of fresh electrode, and the situation are contrary when the current density exceeds the boundary, corresponding well with the changes of the CP plots discussed above.

The energy density and power density characteristics of an electrode are important in evaluating its performances and commercial specifications for electrochemical capacitors. Figure 13a, b show plots of energy density and power density of the $NiCo_2O_4$ electrode determined from CP plots, respectively. As shown in the figure, both energy density and power density in fresh display a approximate linear ascending trend with increase of current density, in that the electrode is in a continuous active state with increase of current density. However, after 5,000 cycles, power density still displays a linear ascending slope whereas energy density exhibits a descending gradient with the increase of current density, indicating the contradiction of the

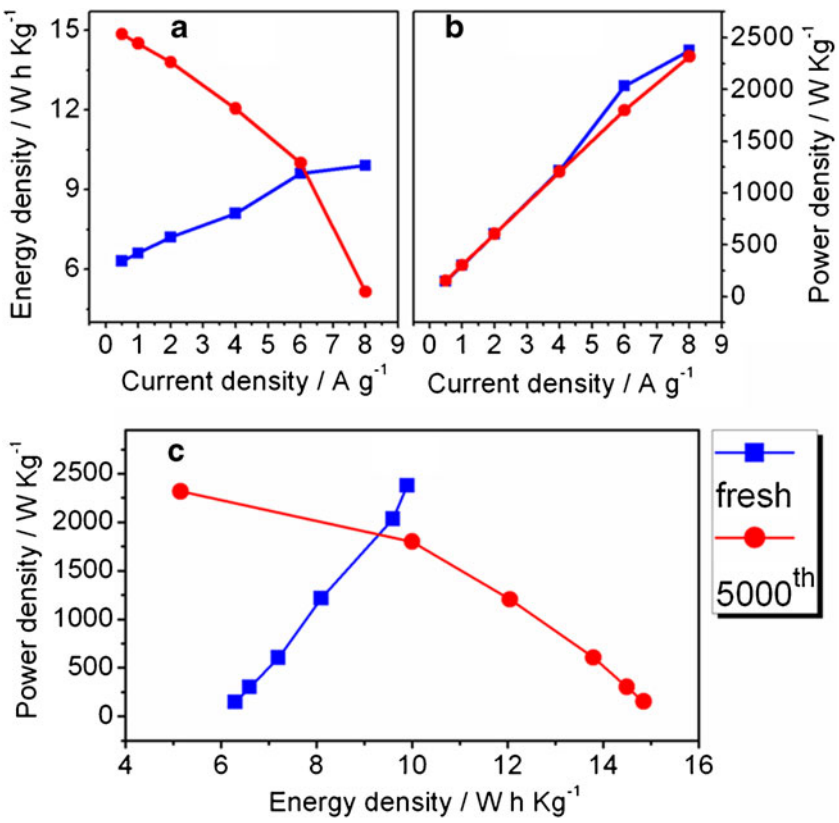

Fig. 13 Energy density and power density performances of $NiCo_2O_4$ electrode in fresh and after 5000 cycles: variations of energy density (**a**) and power density (**b**) with current density, and Ragone plots (**c**)

electrode to deliver energy and power synchronously as most of electrode materials do. The Ragone plots in Fig. 13c summarize the performance of the electrode at various current densities. As illustrated in the figure, in fresh, the power density increases from 146.3 to 2,033 Wkg^{-1} when energy density increases from 6.3 to 9.9 Wh kg^{-1}, while after 5,000 cycles, the power density increases from 153.2 to 2,318 Wkg^{-1} when energy density decreases from 14.85 to 5.15 Wh kg^{-1}. Based on the result, we can see that the electrode is capable of delivering high power but without profound loss in energy, indicating a promising application in electrochemical capacitors.

Conclusions

Mesoporous $NiCo_2O_4$ nanoparticles were synthesized via a facile and cost-effective ball milling solid-state method and followed by a simple thermal treatment. The obtained materials consist of nanostructured $NiCo_2O_4$ spinels of hexagonal morphology and a spot of nanosized NiO spherical particles and display a mesoporous structure. The $NiCo_2O_4$ electrode exhibits mainly a Faradaic pseudocapacitive behavior and possesses high performance even after 5,000 cycles with high specific capacitance (554 Fg^{-1} at 2 mV s^{-1}), high power density and energy density (2,318 W kg^{-1} and 5.15 Wh kg^{-1} at 8 Ag^{-1}), excellent cycling behavior with no capacitance decays and high coulombic efficiency close to 100 % during 5,000 cycles, indicating a promising application for electrochemical capacitors.

Acknowledgments We gratefully acknowledge the financial support of this research by National Basic Research Program of China (2012CB932800 and 2011CB935702), Scientific Research Foundation for the Returned Overseas Chinese Scholars and State Education Ministry (SRF for ROCS, SEM) and Hundred Talents Program of Chinese Academy of Sciences.

References

1. Aricò AS, Bruce P, Scrosati B, Tarascon JM, Van Schalkwijk W (2005) Nat Mater 4:366–377
2. Liu C, Li F, Ma LP, Cheng HM (2010) Adv Mater 22:E28–E62
3. Simon P, Gogotsi Y (2008) Nat Mater 7:845–854
4. Esposito DV, Hunt ST, Stottlemyer AL, Dobson KD, Mc Candless BE, Birkmire RW, Chen JG (2010) Angew Chem 122:10055–10058, (2010) Angew Chem Int Ed 49:9859–9862
5. Burke A (2000) J Power Sources 91:37–50
6. Zheng JP, Cygon PJ, Jow TR (1995) J Electrochem Soc 142:2699–2704
7. Zheng YZ, Ding HY, Zhang ML (2008) Thin Solid Films 516:7381–7385
8. Chang JK, Lin CT, Tsai WT (2004) Electrochem Commun 6:666–671
9. Subramanian V, Zhu H, Vajtai WR (2005) J Phys Chem B 109:20207–20214
10. Kuo C, Mare AA (1996) J Electrochem Soc 143:124–130
11. Yuan CZ, Gao B, Su LH, Zhang XG (2008) Solid State Ion 178:1859–1866
12. Gao YY, Chen SL, Cao DX (2010) J Power Sources 195:1757–1760
13. Xiong SL, Yuan CZ, Zhang XG, Xi BJ, Qian YT (2009) Chem Eur J 15:5320–5326
14. Tarasevich MR, Efremov BN, Trasatti S (eds) (1982) Electrodes of conductive metallic oxides, part A. Elsevier: USA
15. Verma S, Joshi HM (2008) J Phys Chem C 112:15106–15112
16. Marsan B, Fradette N, Beaudoin G (1992) J Electrochem Soc 139:1889–1896
17. Singh RN, Koenig JF, Chartier GP (1991) J Electroanal Chem 314:241–257
18. Roginskaya YE, Morozova OV, Lubnin EN, Ulitina YE, Lopukhova GV, Trasatti S (1997) Langmuir 13:4621–4627
19. Haenen J, Visscher W, Barendrecht E (1986) J Electroanal Chem 208:273–341
20. Windisch CFJ, Ferris KF, Exarches GJ (2001) J Vac Sci Technol, A 19:1647–1651
21. Windisch CFJ, Exarhos GJ, Sharma SK (2002) J Appl Phys 92:5572–5574
22. Chadwick AV, Savin SLP, Fiddy S, Alcantara R, Lisbona DF, Lavela P, Ortiz GF, Tirado JL (2007) J Phys Chem C 111:4636–4642
23. Alcntara R, Jaraba M, Lavela, Tirado JL (2002) Chem Mater 14:2847–2848
24. Cui B, Lin H, Liu Y, Li J, Sun P, Zhao XC, Liu CJ (2009) J Phys Chem C 113:14083–14087
25. Marco JF, Gancedo JR, Gracia M, Gautier JL, RmHos E, Berry FJ (2000) J Solid State Chem 153:74–81
26. Cabo M, Pellicer E, Rossinyol E, Castell O, Surinach S, Baro MD (2009) Cryst Growth Des 9:4814–4821
27. Gupta V, Gupta S, Miura N (2010) J Power Sources 195:3757–3760
28. Verma S, Joshi HM, Jagadale T, Chawla A, Chandra R, Ogale S (2008) J Phys Chem C 112:15106–15112
29. Klissursk DG, Uzunova EL (1991) Chem Mater 3:1060–1063
30. Kim JG, Pugmire DL, Battaglia D, Langell MA (2000) Appl Surf Sci 162:70–84
31. Wei TY, Chen CH, Chien HC, Lu SY, Hu CC (2010) Adv Mater 22:347–351
32. Salunkhe RR, Jang K, Yu H, Yu S, Ganesh T, Sung-Hwan Han HA (2011) J Alloys Compd 509:6677–6682
33. Wu YQ, Chen XY, Ji PT, Zhou QQ (2011) Electrochim Acta 56:7517–7522
34. Kandalkar SG, Lee HM, Seo SH, Lee K, Kim CK (2011) Korean J Chem Eng 28:1464–1467
35. Wang HW, Hu ZA, Chang YQ, Chen YL, Wu HY, Zhang ZY, Yang YY (2011) J Mater Chem 21:10504–10512
36. Wang CH, Zhang X, Zhang DC, Yao C, Ma YW (2012) Electrochim Acta 63:220–227
37. Chi B, Li JB, Han YS, Chen YJ (2004) Int J Hydrogen Energy 29:605–610
38. Peshev P, Toshev A, Gyurov G (1989) Mater Res Bull 24:33–40
39. Lapham DP, Tseung ACC (2004) J Mater Sci 39:251–264
40. Kim JG, Pugmire DL, Battaglia D, Langell MA (2000) Appl Surf Sci 165:70–84
41. Marco JF, Gancedo JR, Gracia M, Gautier JL, Rios E, Berry FJ (2000) J Solid State Chem 153:74–81
42. Thissen A, Ensling D, Fernandez Madrigal FJ, Jaegermann W, Alcantara R, Lavela P, Tirado JL (2005) Chem Mater 17:5202–5208
43. Zhou H, Li D, Hibino M, Honma I (2005) Angew Chem Int Ed 44:797–802

44. Hu CC, Chang KH, Lin MC, Wu YT (2006) Nano Lett 6:2690–2695
45. Futaba DN, Hata K, Yamada T, Hiraoka T, Hayamizu Y, Kakudate Y, Tanaike O, Hatori H, Yumura M, Iijima S (2006) Nat Mater 5:987–994
46. Choi D, Blomgren GE, Kumta PN (2006) Adv Mater 18:1178–1182
47. Justin P, Meher SK, Ranga Rao G (2010) J Phys Chem C 114:5203–5210
48. Hu CC, Chang KH, Hsu TY (2008) J Electrochem Soc 155:F196–F200
49. Wu YT, Hu CC (2004) J Elecrochem Soc 151:A2060–A2066
50. Srinivasan V, Weidner JW (2000) J Electrochem Soc 147:880–885
51. Lust E, Janes A, Arulepp M (2004) J Electroanal Chem 562:33–42
52. Taberna PL, Simon P, Fauvarque JF (2003) J Electrochem Soc 150:A292–A300
53. Ganesh V, Pitchumani S, Lakshminarayanan V (2006) J Power Sources 158:1523–1532
54. Adekunle AS (2011) Ozoemena KI Electroanalysis 23:971–979
55. Mermilliod N, Tanguy J, Petior F (1986) J Electrochem Soc 133:1073–1079
56. Tanguy J, Mermilliuod N, Hoclet M (1987) J Electrochem Soc 134:795–802
57. Kalaji M, Peter LM (1991) J Chem Soc Faraday Trans 87:853–860
58. Feldman BJ, Burgmayer P, Murray RW (1985) J Am Chem Soc 107:872–878
59. Cole KS, Cole RH (1941) J Chem Phys 9:341–351